MATERIALS SCIENCE

Imaging of the electronic bonding of diamond at pressures up to 2 million atmospheres

Sung Keun Lee[1,2]*†, Yoosoo Yi[1]†, Yong-Hyun Kim[1], Hyo-im Kim[1], Paul Chow[3], Yuming Xiao[3], Peter Eng[4], Guoyin Shen[3]

Diamond shows unprecedented hardness. Because hardness is a measure of resistance of chemical bonds in a material to external indentation, the electronic bonding nature of diamond beyond several million atmospheres is key to understanding the origin of hardness. However, probing the electronic structures of diamond at such extreme pressure has not been experimentally possible. The measurements on the inelastic x-ray scattering spectra for diamond up to 2 million atmospheres provide data on the evolution of its electronic structures under compression. The mapping of the observed electronic density of states allows us to obtain a two-dimensional image of the bonding transitions of diamond undergoing deformation. The spectral change near edge onset is minor beyond a million atmospheres, while its electronic structure displays marked pressure-induced electron delocalization. Such electronic responses indicate that diamond's external rigidity is supported by its ability to reconcile internal stress, providing insights into the origins of hardness in materials.

INTRODUCTION

The origin of the exceptional rigidity of diamond at 1 atm and under extreme compression remains to be explored. Superhard diamond undergoes structural densification upon extreme pressure (*1*, *2*), and the nature of the C—C bond in the compressed diamond above megabar (million atmosphere) pressure is expected to be different from that at ambient pressure. Therefore, the detailed pressure-driven change in diamond's electronic structure and the electronic density of states (DOS) at high pressure yield insights into the origin of the diamond's pronounced hardness. This is because the pressure-induced evolution of DOS results from the modification of electron distribution in C—C bond upon compression and the hardness of a material is based on its chemical bonds' resistance to external indentation and densification. Compressed diamonds in the Earth's interior also help us to infer the distribution of deep carbon (*3*–*7*) and serve as a window into the planetary interior (*8*–*10*). The studies of diamond under multimegabar conditions also allow us to clarify the evolution of carbon-rich exoplanets whose masses are several times that of the Earth [see (*11*) and references therein]. Extensive efforts have been made to unveil the nature of diamond under extreme pressure [e.g., (*1*, *12*–*16*)]. Structural deformation in diamond at high pressure has been explored using x-ray diffraction (*17*–*19*), constraining its electronic and optical properties (*20*). While elastic x-ray scattering provides lattice structures, the local electronic bonding environment around carbon in diamond at high pressure, particularly above a megabar is unknown as in situ experimental probing of the detailed nature of C—C bond in densified diamond is challenging.

Inelastic x-ray scattering (IXS) probes core electron excitations from low-Z elements like carbon and has provided changes in the electronic DOS under extreme pressure [see (*21*–*26*) and references therein]. In particular, carbon K-edge IXS shows structural transitions and the prevalence of sp^3 carbon in amorphous carbon and graphite at high pressure (*21*, *27*). However, bonding transitions in diamond above megabar pressures have not been experimentally probed as inelastic x-ray signal intensity is often 10^{-4} to 10^{-6} of that of elastic x-rays. As the pressure increases, background signals from the anvils used to confine matter increase during IXS measurement. While the overwhelming background from anvil makes it difficult in identifying structural changes of confined matter with IXS above 100 GPa, we can turn it to our benefit by tracing the bonding transition in a compressed diamond anvil itself. In this study, we intentionally irradiated the tip of the diamond anvil near the culet compressed above megabar pressure conditions. Together with a polycapillary postscattering collimator (*28*–*30*), collection of the IXS signal from the focused volume of diamond is achieved (see Materials and Methods and supplementary text A for further details of scattering geometry). These factors led to a much improved spatial resolution within the diamond anvil, opening a window to investigate the pressure-driven electronic bonding transitions and DOS of diamond. The ability to probe the DOS is key to direct estimation of the pressure-induced evolution of electronic structures that reveal the origin of the diamond's incompressibility. The probing of its electronic structure also makes it suitable as a useful pressure indicator above 100 GPa, as the pressure determination at megabar pressure conditions has remained difficult [see (*31*) for a review]. In the current study, we report the carbon K-edge IXS spectra and the two-dimensional IXS mapping of the electronic bonding structure of diamond beyond megabar pressures.

RESULTS

The carbon K-edge IXS spectra for diamond up to 200 GPa reveal the evolution of the electronic structure around carbon upon extreme compression (Fig. 1). The IXS spectrum for diamond at 1 atm shows an absorption edge (E_0) at 289.5 eV and four major features at 291.3 (P1), 297.5 (P2), 305.1 (P3), and 307.5 (P4) eV that are

[1]School of Earth and Environmental Sciences, Seoul National University, Seoul 08826, Korea. [2]Institute of Applied Physics, Seoul National University, Seoul, Korea. [3]HPCAT, X-ray Science Division, Argonne National Laboratory, Argonne, IL 60439 USA. [4]Center for Advanced Radiation Sources, The University of Chicago, Chicago, IL 60637, USA.
*Corresponding author. Email: sungklee@snu.ac.kr
†These authors contributed equally to this work.

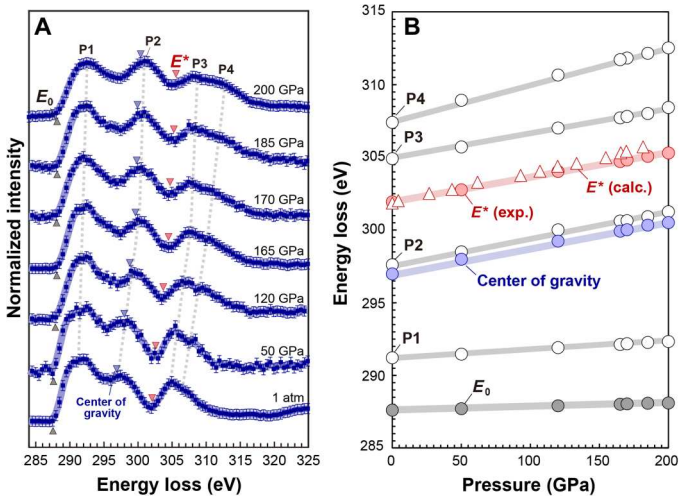

Fig. 1. Evolution of electronic bonding structures of diamond with pressure up to 2 Mbar. (**A**) Carbon K-edge inelastic x-ray scattering (IXS) spectra for diamond with increasing pressure up to 200 GPa. The IXS spectra spectral intensity is plotted with respect to the energy loss (i.e., incident energy – elastic energy). (**B**) Effect of pressure on peak positions [second bandgap (E^*), center of gravity (E_c), and characteristic peak positions of the σ* pattern].

characteristics of the transition of a 1s electron to a virtual σ* orbital for sp^3-bonded $^{[4]}$C (Fig. 1A), which is consistent with earlier 1*s* core-level excitation spectra for diamond [e.g., (*32*–*35*)]. The σ* features at 1 atm are characteristically divided by the prominent gap at ~302 eV (also known as the second bandgap, E^*) (*36*). With increasing pressure up to ~200 GPa, a gradual and linear shift in the main σ* peak and E^* is observed (Fig. 1B). The pressure-induced increase in the edge onset energy (E_0) and the center of gravity (E_c) of the full spectrum, as well as the peak positions (from E^*, P1 to P4) of IXS features, are also evident (supplementary text B). In addition to positive shifts with pressure, the main σ* features become broader with increasing pressure as shown in the noticeable increases in the energy difference between the features. For instance, the difference in energy between P3 and P4 increases from 2.4 (at ambient pressure) to 4.2 eV (at 200 GPa); the pressure-induced peak shift is smallest for P1 and becomes largest for P4 (Fig. 1B). Such trends indicate an increase in electronic dispersion upon compression.

Theoretical ab initio calculations of the carbon K-edge IXS spectra (i.e., unoccupied DOS) for diamond up to ~2 Mbar provide the electronic origins of the pressure-driven evolution of σ* feature [see supplementary texts C1 to C6 for detailed results and calculation conditions]. As the current IXS experimental setup results in an anisotropic compression of the diamond anvil, ab initio calculations were performed for diamond with strain ratios from hydrostatic ($\varepsilon_{11}/\varepsilon_{33} = 1$) to uniaxial compression ($\varepsilon_{11}/\varepsilon_{33} < 1$) (supplementary texts A and B). The calculated IXS peaks shift to higher energy with pressure (supplementary texts B and C1 to C3), consistent with the experimental results. Our calculations of the electronic structures also include bandgap (E_g) of diamond both under hydrostatic and uniaxial compression (supplementary texts B and C). Upon hydrostatic compression, the E_g (and thus, the shift in 1*s* electron excitation energy] of the compressed diamond increases gradually with increasing pressure ($E_g = 0.0030 \times P + 4.19$). Upon uniaxial compression, the E_g decreases linearly with pressure, and the detailed trends depend on the degree to which the crystal is uniaxially compressed (supplementary texts B and C). Observed changes are described with linear pressure dependence, indicating rather gradual change in electronic transitions in diamond with increasing pressure (see tables in supplementary texts B and C). These compare well with the observed linear pressure changes in σ* DOS in diamond under compression up to 2 Mbar (Fig. 1). As the equation of state (EOS) from static x-ray study for diamond is available up to ~140 GPa (*37*), the pressure conditions beyond 140 GPa were obtained by extending the EOS to ~200 GPa and also calculated from the internal stress (supplementary text A). We use both pressure values to show the effect of pressure on the peak shifts of the σ* features.

Figure 2 shows the pressure-driven changes in E^* and E_0 in the experimental and theoretical C K-edge IXS spectra up to 2 Mbar. First, our simulations show that E_0 position somewhat depends on the nature of anisotropic compression and scattering geometry, which allows to infer the nature of diamond compression (see supplementary text C4); as the calculated E_0 under hydrostatic (and uniaxial) compression increases (and decreases) with pressure, the experimental ΔE_0 appears to be similar to the predicted trend for hydrostatic compression (Fig. 2A). However, the calculated IXS patterns with varying scattering geometry [i.e., scattering vector (*q*) perpendicular to ($q \perp c$) and parallel ($q \parallel c$) to the compression axis, *c*] confirm that the experimental trend in Fig. 1 is best explained by the IXS with $q \perp c$ geometry under uiaxial compression. This is consistent with the current experimental setting where *q* is perpendicular to <001> direction of diamond anvils under uniaxial compression (Fig. 2B) (see supplementary texts C4 to C6 for detailed scattering geometry).

The observed shifts in the IXS patterns (e.g., E^* in Fig. 1B) stem mainly from contraction of the C—C bond distance [d(C—C)] and the accompanying electron delocalization. Our ab initio simulations of diamond both under hydrostatic and uniaxial compression reveal the shortening of d(C—C) with pressure (Fig. 2C; supplementary text C3); at constant pressure, while the next-nearest d(C—C) changes and bifurcates with increasing anisotropic strain, the nearest d(C—C) does not change notably with varying degrees of anisotropic compression [e.g., at 113 GPa, 1.4536 Å (hydrostatic); 1.4549 Å ($\varepsilon_{11}/\varepsilon_{33} = 0.33$); supplementary text C3]. An observed E^* peak shift in diamond up to ~188 GPa corresponds to a decrease in the nearest d(C—C) of ~0.134 Å (Fig. 2D). Except those for near-edge features (E_0 and P1), the K-edge peak positions (E^*, E_c, and P2 to P4) are not substantially affected by the varying degree of anisotropic compression and correlates with pressure (supplementary text C4). In particular, the E^* position systematically shifts with increasing pressure (Figs. 1 and 2D), which can be described by the linear equation: $E^*(P) = 0.0168 \times P + 301.93$ (Fig. 2D). This indicates that E^* of compressed diamond serves as a reliable pressure gauge (see below for further discussion).

As shown in Figs. 1 and 2, the change in IXS features becomes more pronounced the further away they are from the edge onset (E_0). Therefore, the changes in diamond's overall IXS patterns during compression are dominated by dispersion of σ* states, rather than a shift in E_0. This behavior is in contrast to those observed for much softer materials (*24*, *29*); earlier experimental measurements and theoretical calculations of IXS spectra for diverse materials (e.g., SiO_2, $MgSiO_3$, and B_2O_3) above 100 GPa show that the E_0 increases systematically with increasing pressure, and

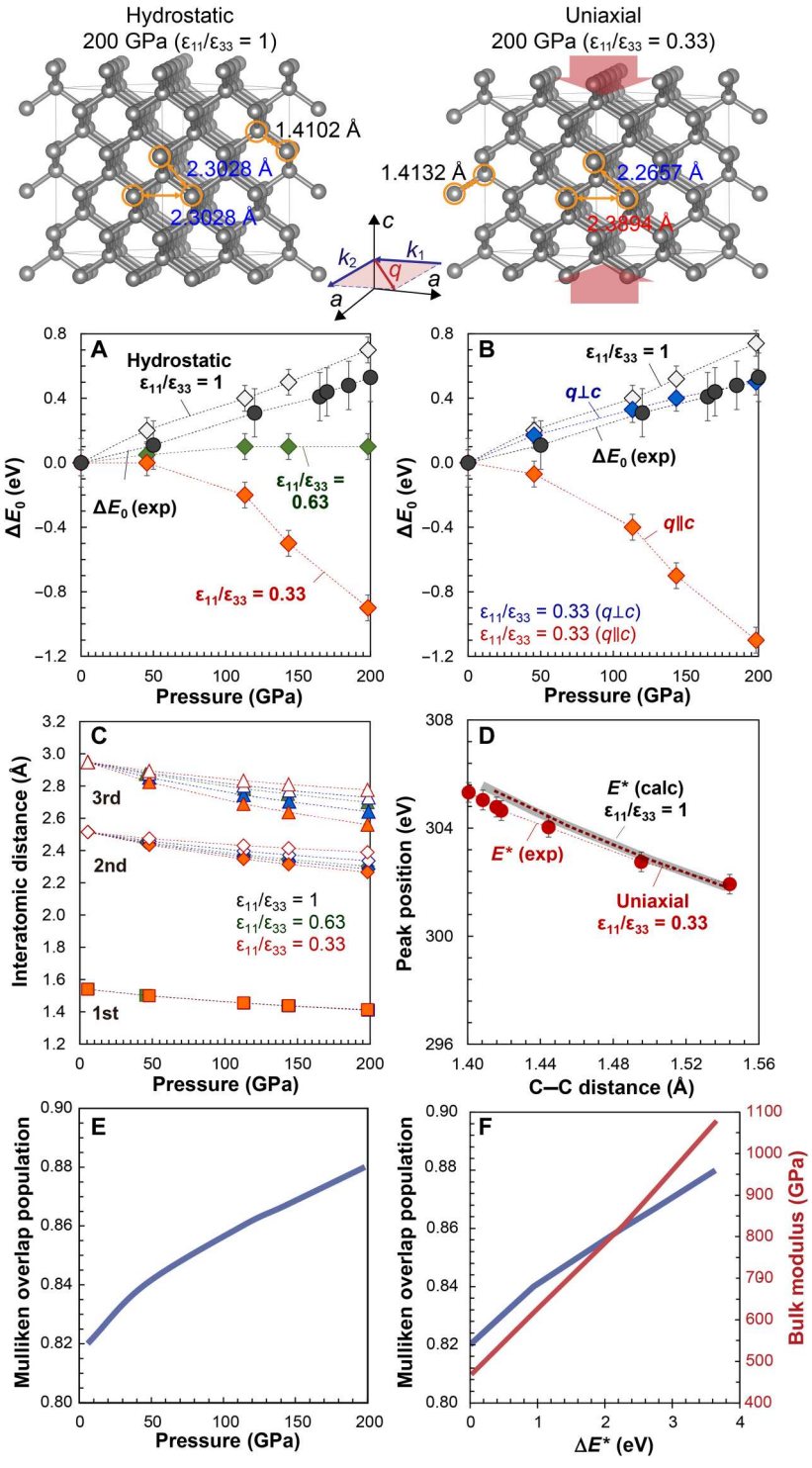

Fig. 2. Pressure-induced changes in lattice and electronic structures, IXS patterns, and bulk modulus of diamond. (Top) Lattice structures of diamond at 200 GPa with varying degrees of anisotropic compression with $\varepsilon_{11}/\varepsilon_{33}$ = 1 (hydrostatic, left) and $\varepsilon_{11}/\varepsilon_{33}$ = 0.33 (uniaxial, right). The interatomic distances between the first and second nearest-neighbor carbons are shown. (**A**) Pressure-induced changes in the edge energy onset [$\Delta E_0 = E_0(P) - E_0(1\text{atm})$] for hydrostatically and uniaxially compressed diamond with varying anisotropic stain ($\varepsilon_{11}/\varepsilon_{33}$) (see supplementary texts C1 to C6). Upon uniaxial compression, E_0 decreases, and the detailed trends depend on the degree to which the crystal is compressed. Black circles show experimental results. (**B**) Pressure-induced changes in the edge energy onset for uniaxially compressed diamond with varying scattering geometry ($q \perp c$ and $q \parallel c$). (**C**) Variation in the interatomic distance between the first-, second-, and third-order nearest-neighbor carbons with pressure and $\varepsilon_{11}/\varepsilon_{33}$; the C—C distance based on hydrostatic compression (black); uniaxial compression with $\varepsilon_{11}/\varepsilon_{33}$ = 0.63 (blue) and with $\varepsilon_{11}/\varepsilon_{33}$ = 0.33 (red). (**D**) Effect of pressure on E^* and nearest neighboring C—C length with varying degree of anisotropic compression [$\varepsilon_{11}/\varepsilon_{33}$ of 1 and 0.33]. The pressure values from the extended EOS (red) (*37*) and those calculated from the internal stress (blue) are shown (see supplementary texts C1 to C6). Red circles denote E^* of the experimental IXS spectrum. (**E**) Effect of pressure on Mulliken overlap population (MOP) (supplementary text E). (**F**) Relationship among MOP, bulk modulus, and ΔE^* [$=E^*(P) - E^*(1\text{ atm})$] of compressed diamond (supplementary text E). The figure in the inset shows the scattering geometry ($q \perp c$) of the experiment (supplementary text C5).

the magnitude of such a positive shift in the edge energy is comparable to the pressure-induced overall shift at the center of gravity of the σ* feature of these oxides under compression above megabar pressures (*28*). For example, the σ* shift (measured at the center of gravity, E_c) are primarily attributed to an increase in E_0 (~2 to 3 eV/100 GPa for $MgSiO_3$-bridgmanite and SiO_2 phases), without noticeable changes in the width of the IXS pattern, confirming that the pressure-driven evolution in DOS is controlled by the E_0 shift (see supplementary text D). In contrast, our IXS results for the hydrostatically compressed diamond show that the edge energy shift is minor (~0.3 eV/100 GPa), yet the pressure-induced changes at the center of gravity of σ* and E^* are prevalent (~2 to 2.5 eV/100 GPa for peak shift of E_c, E^*, and P4, see supplementary text D). Together with the pressure-induced increase in spectral width (Fig. 1), the

results highlight flexible overall changes in the DOS pattern of diamond due to electron dispersion under densification. Considering the vertical beam size with full width at half maximum (FWHM) of ~3 μm and the overall scattering volume determined mainly from a spatial resolution along the x-ray paths (see supplementary text A), the IXS spectrum near the culet may capture signals with varying pressure conditions. Such pressure gradient may increase with increasing pressure, which could partly contribute to a broadening of the spectral features. Nevertheless, the magnitude of spectral dispersion in the experimental spectra up to 2 Mbar is similar to that in theoretical spectrum (supplementary texts B and C4), indicating that the pressure-induced dispersion is intrinsic to the compressed diamond.

The observed trends enable us to postulate that diamond's incompressibility can be explained by the observed DOS pattern with pressure. In particular, the relatively small change in the E_0 beyond megabar pressures may result from the resistance of d(C—C) contraction of under compression. The marked increase in electronic dispersion as evidenced by ~2 eV/100 GPa increase in E^* attributes to the exceptional rigidity of diamond under compression [e.g., with its bulk modulus from 466 (at ~6 GPa) to 825 GPa (at ~113 GPa)] (supplementary texts D and E) (*38*), while more extensive efforts are necessary to corroborate our postulate of the IXS pattern as a window into materials' incompressibility.

Bulk modulus of superhard covalent solids with incompressibility has strong correlation with intrinsic hardness as both properties record the resistance in change in bond length upon compression [e.g., (*39*)]. Incompressibility of superhard materials mainly stems from the strength of chemical bond (see supplementary text E for relationship between hardness, bulk modulus, and electronic DOS in diamond). The intrinsic hardness has been reported to correlate with electronic bond density, bandgap, and enhanced Mulliken overlap populations (MOPs) [see (*40*–*45*) and references therein; supplementary text E4]. All these bond properties correspond to how DOS pattern evolves as it represents the collective nature of chemical bonding and bond strength. As the MOP has been correlated with the bulk modulus of materials (*45*), the observed pressure-induced increase in MOP corresponds to an increase in its incompressibility (Fig. 2E), mainly due to manifested pressure-induced electronic dispersion (Fig. 1). As shown in supplementary text E4, the pressure-induced increase in electronic dispersion in electronic 1s excitation in the unoccupied DOS spectra of diamond at high pressure is also linked to a shift in E^* position. Therefore, the diamond's exceptional incompressibility under compression can also be parameterized by ΔE^* (Fig. 2F). While the strong covalent bonding in diamond has been attributed to its exceptional hardness, the detailed evolution of DOS with pressure yield complimentary electronic insights into the nature of incompressibility upon extreme compression.

The position of E^*, together with other characteristic peaks, can be used as a spectral proxy of the diamond densification based on IXS. While the Raman peak shift for the diamond edge has been effective in estimating the pressure within a diamond anvil at high pressure (*46*), the validity of the Raman scale needs further refinement, particularly above 150 GPa, and additional accurate pressure scales operating above megabar pressures are anticipated (*31*, *47*–*49*). The peak positions for distinct σ* features and the second bandgap also show a linear relationship with the Raman shift (Δ_R) of the diamond anvil edge: $E^*(P) = -97 \times \Delta_R(P) - 27{,}960$ (supplementary text F). Further calibration, potentially with smaller beam is necessary to fully quantify the relationship. Considering aforementioned inefficiency in IXS processes, uncertainty in peak position, its utility as a pressure indicator may rather be limited. Nevertheless, the ~10-keV x-rays used to make the measurement do not induce anvil instability. The current C K-edge IXS pressure gauge with compressed diamond up to 2 Mbar provides a useful way to determine the pressure conditions during IXS experiment.

On the basis of the established relationships between pressure and IXS peak positions (Fig. 2), the pressure conditions within the tip of the compressed anvil can be estimated. As shown in Fig. 3 (bottom), the IXS spectra for the diamond anvil with varying depth from the culet surface exhibit the changes in carbon K-edge E_c and E^* peak positions (and thus pressure) (Fig. 3, top). The shift in the features (from that at 1 atm) decreases with increasing depth (d, micrometers) from the culet surface. For the compressed anvil at 200 GPa, $E^*(d) = 3.5 \times \exp(-0.018\times d) + 301.93$, which indicates that the culet surface shows the highest pressure, and the pressure condition exponentially decreases with increasing depth from the culet surface [i.e., for a diamond anvil at 200 GPa, pressure(d) = $200 \times \exp(0.018 \times d)$]. Notably, the pressure within the culet is mostly released beyond 200 μm from the culet surfaces, consistent with the concept of partially perforated diamond anvils. The internal stress is therefore localized within 200 μm of the culet tip, a further illustration of incompressibility of diamond. The extent of anisotropic compression may vary with depth from the culet surface. While the change may be experimentally observed in edge onset (E_0) with a scattering geometry with $q \| c$ (supplementary text C), the current scattering geometry does not show the variation in potential changes in anisotropic compression with depths. We also point out that the E^* position does not vary with varying degree of anisotropic compression.

The simple relationships between IXS features and pressure open a way to probe the deformation behavior of compressed diamond; as the beam size [with FWHM of 5 [horizontal (h)] μm by 3 [vertical (v)] μm] is sufficiently small, the depth and horizontal profile of the diamond can be resolved, allowing us to obtain the stress distribution within the diamond anvil. Figure 4 presents a two-dimensional image of the deformed diamond anvil at 120 GPa. Here, the image is constructed on the basis of the E^* position with pressure (Figs. 1 and 2). The image confirms that the tip of the anvil reaches the highest pressures and that the pressure decreases with increasing distance from the tip of the anvil. Considering the relationship between C—C bond length and pressure (Fig. 2), the reduction in C—C bond becomes prominent near the culet (Fig. 3). This demonstrates that the tip of the diamond anvil under compression stores a moderate amount of elastic energy. Stress is also horizontally localized within ~120 μm, which is comparable to the size of the culet, revealing details of the bonding nature within the compressed diamond anvil. These in situ stress maps can be used to validating finite element analysis stress models of the truncated brilliant cut diamond under load and could potentially be helpful in suggesting improved tip geometries that increase the maximum achievable pressure before the diamond breaks. The two-dimensional maps of IXS peak intensity also reveal the shape of diamond culet under 120 GPa where the deformation is concentrated below the culet (Fig. 4, center). The IXS results shed light on the rare

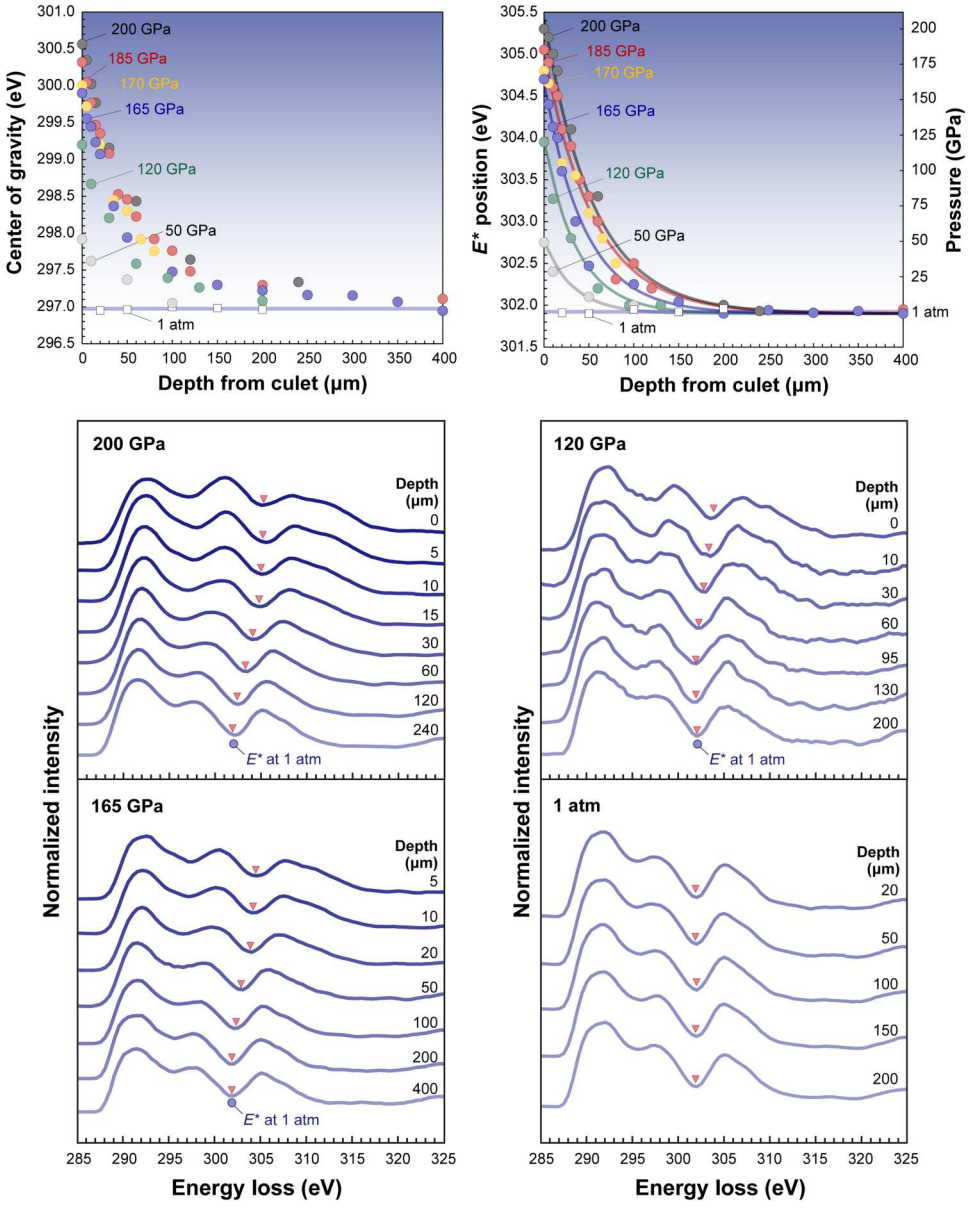

Fig. 3. The pressure-driven changes in carbon K-edge features for diamond with varying depth from the culet surface. (Top) The pressure-induced changes in the peak positions for center of gravity and the second bandgap with varying pressure and varying depth from the culet surface. (Bottom) Carbon K-edge IXS spectra for diamond with varying depth from the culet surface at high pressure as labeled.

opportunity to image the electronic structures of materials under extreme deformation and pressure.

DISCUSSION

While the detailed electronic bonding nature of diamond at high pressure had not been experimentally probed, the current study highlights an in situ IXS measurement for diamond above megabar pressure conditions up to 200 GPa—the current high pressure record for experimental nonresonant (x-ray Raman) IXS studies, directly probing the evolution of bonding transitions in diamond up to multimegabar. The linear relationships between C K-edge peak shifts (including the second bandgap) and pressure provide a predictive spectral proxy with the compressed diamond anvil. With such advances, this study reports the in situ two-dimensional image of the electronic bonding transitions with full DOS of any condensed matter, not to mention diamond undergoing densification above 1 Mbar. The pressure distribution in the anvil follows an exponential function with increasing depth from the culet surface, as the stress is mostly localized near the tip, regardless of the maximum pressure up to 2 Mbar. As IXS is becoming a widely used technique at synchrotron x-ray sources and will become more accessible with improved x-ray optics in the future, the established pressure dependence of E^* with further refinement may be a useful pressure indicator for future IXS studies beyond multimegabar pressures relevant to deep super-Earth bodies

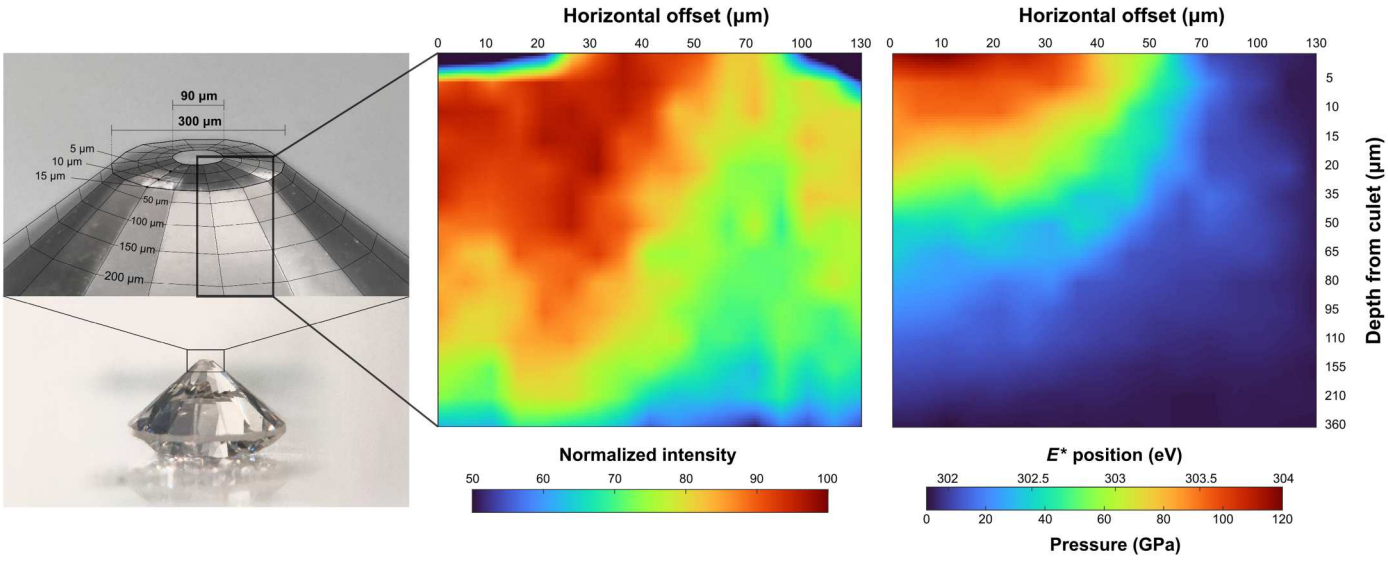

Fig. 4. Carbon K-edge IXS spectral image for diamond at 120 GPa. (Left) The diamond anvil (modified brilliant cut diamond) used for the current study. (Center) Two-dimensional image of C K-edge IXS spectral intensity (i.e., normalized intensity of IXS peak for P1 with respect to that at ~60 μm in depth at zero horizontal offset) with the maximum intensity where the shape of the compressed diamond can be seen. (Right) Carbon K-edge IXS spectral image for diamond at 120 GPa based on the *E** peak position (the images here are scaled in that the sizes of the pixels are not identical; see supplementary text G for the unscaled images).

(supplementary text F for the assessment of the practical utility of the protocol). The current IXS results may unveil the underlying mechanism of diamond's hardness; its incompressibility upon densification is manifested in minor changes in IXS features near the edge onset for diamond under hydrostatic compression beyond a million atmospheres (supplementary texts C1 to C6 and D). Nevertheless, the overall electronic structure exhibits greater flexibility at external pressure, highlighted by marked pressure-induced shift and electron delocalization in σ* features in full DOS pattern, distinct from those observed for other "softer" materials. We postulate that the observed dispersion is likely to contribute their resistance to deform under extreme pressure conditions. Such dual electronic responses (a minor change in edge energy onset and pronounced dispersion and thus flexibility in extended DOS) of sp^3 bond during compression further characterize the diamond's ability to reconcile internal stress and therefore its high bulk modulus. These unique evolutions of electronic structures account for diamond's unprecedented hardness and rigidity under extreme compression. The information on the pressure-driven changes in the DOS pattern proved by C K-edge may be useful to explore the electronic origins of hardness and rigidity in diverse materials.

MATERIALS AND METHODS

Synchrotron IXS experiment

A modified panoramic diamond anvil cell with Be gasket was used with the diamond culet of ~110 μm for low-pressure experiment up to 120 GPa and those of 90 μm from 165 to 200 GPa. We used the modified brilliant cut diamond anvils where its <001> axis is aligned parallel to the compression axis. Carbon K-edge IXS spectra for the compressed diamond anvil tip from the culet surfaces were collected at the Advanced Photon Source [beamline 16-ID-D of high-pressure collaborative access team (HPCAT)] (see supplementary text A for experimental details). During the IXS spectrum collection of the compressed diamond anvil with varying pressures from 1 atm to 200 GPa, the monochromatic x-rays with the FWHM of ~5 (*h*) μm by ~3 (*v*) μm were focused to the tip of the anvil. The intensity of the inelastically scattered photons from the diamond anvils near the culet surfaces was counted with varying incident beam energy relative to 9.9047 keV (the analyzer energy). Postcollimation of the photons was achieved using polycapillary optics [see (*28*, *29*, *50*, *51*) for the details] with a scattering angle of 25°. Horizontal and vertical profile of the anvil tip was scanned by moving the diamond anvil cell (DAC) position. The Raman pressure scale of the diamond culet was used (*46*), which was then correlated with the observed IXS peak shift.

Ab initio calculations of IXS spectra for diamond at high pressure

The carbon K-edge IXS spectra and σ* DOS (i.e., double differential scattering cross section, describing electronic transition from 1s to virtual states) for diamond at high pressure were calculated from the core electron excitation spectroscopy module in the CASTEP code (*52*). To explore the densification of diamond structures, we varied the lattice parameter from 3.5560 to 3.2004 Å (i.e., 1.0–0.7290V_0 in volume); the estimated internal stress increased up to ~220 GPa. We investigated the electronic structures of hydrostatically compressed diamond and explored two distinct cases of anisotropic compression. See supplementary texts C1 to C6 for detailed calculated lattice structures of the compressed diamond used. The electronic structure calculations were performed without further geometry optimizations. The projector augmented wave–type pseudopotential method with the on-the-fly scheme was used. The IXS spectra were calculated by considering the core-hole effect on a target C atom in unit cell. The Perdew-Berke-Ernzerhof exchange-correlation functional with the generalized gradient approximation (GGA) was used to evaluate the short-range electronic interactions. The plane-wave cutoff energy was 800 eV (supplementary text A for

additional calculation details). The IXS spectra of compressed diamonds were calculated by applying the final state approximation. The 2 × 2 × 2 supercell structure containing 108 carbon atoms was used. The current ab initio calculations enable estimation of the quantitative effect of pressure on the σ* peak shift.

Supplementary Materials

This PDF file includes:

Supplementary texts A to G
Figs. S1 to S29
Tables S1 to S6
References

REFERENCES AND NOTES

1. A. Lazicki, D. McGonegle, J. R. Rygg, D. G. Braun, D. C. Swift, M. G. Gorman, R. F. Smith, P. G. Heighway, A. Higginbotham, M. J. Suggit, D. E. Fratanduono, F. Coppari, C. E. Wehrenberg, R. G. Kraus, D. Erskine, J. V. Bernier, J. M. McNaney, R. E. Rudd, G. W. Collins, J. H. Eggert, J. S. Wark, Metastability of diamond ramp-compressed to 2 terapascals. *Nature* **589**, 532–535 (2021).
2. Q. Hu, B. Li, X. Gao, Y. Bi, L. Su, H.-K. Mao, Ultrasound elasticity of diamond at gigapascal pressures. *Proc. Natl. Acad. Sci. U.S.A.* **118**, e2118490118 (2021).
3. C. Anzolini, F. Nestola, M. L. Mazzucchelli, M. Alvaro, P. Nimis, A. Gianese, S. Morganti, F. Marone, M. Campione, M. T. Hutchison, J. W. Harris, Depth of diamond formation obtained from single periclase inclusions. *Geology* **47**, 219–222 (2019).
4. R. M. Hazen, R. T. Downs, A. P. Jones, L. Kah, Carbon mineralogy and crystal chemistry, in *Carbon in Earth,* R. M. Hazen, A. P. Jones, J. A. Baross, Eds. (Reviews in Mineralogy and Geochemistry, Mineralogical Society of America, 2013), vol. 75, pp. 7–46.
5. M. J. Walter, S. C. Kohn, D. Araujo, G. P. Bulanova, C. B. Smith, E. Gaillou, J. Wang, A. Steele, S. B. Shirey, Deep mantle cycling of oceanic crust: Evidence from diamonds and their mineral inclusions. *Science* **334**, 54–57 (2011).
6. O. Tschauner, S. Huang, S. Yang, M. Humayun, W. Liu, S. N. G. Corder, H. A. Bechtel, J. Tischler, G. R. Rossman, Discovery of davemaoite, $CaSiO_3$-perovskite, as a mineral from the lower mantle. *Science* **374**, 891–894 (2021).
7. Z. Zeng, J. Wen, H. Lou, X. Zhang, L. Yang, L. Tan, B. Cheng, X. Zuo, W. Yang, W. L. Mao, H.-K. Mao, Q. Zeng, Preservation of high-pressure volatiles in nanostructured diamond capsules. *Nature* **608**, 513–517 (2022).
8. F. Nestola, N. Korolev, M. Kopylova, N. Rotiroti, D. G. Pearson, M. G. Pamato, M. Alvaro, L. Peruzzo, J. J. Gurney, A. E. Moore, J. Davidson, $CaSiO_3$ perovskite in diamond indicates the recycling of oceanic crust into the lower mantle. *Nature* **555**, 237–241 (2018).
9. E. M. Smith, S. B. Shirey, S. H. Richardson, F. Nestola, E. S. Bullock, J. Wang, W. Wang, Blue boron-bearing diamonds from Earth's lower mantle. *Nature* **560**, 84–87 (2018).
10. O. Tschauner, S. Huang, E. Greenberg, V. B. Prakapenka, C. Ma, G. R. Rossman, A. H. Shen, D. Zhang, M. Newville, A. Lanzirotti, K. Tait, Ice-VII inclusions in diamonds: Evidence for aqueous fluid in Earth's deep mantle. *Science* **359**, 1136–1139 (2018).
11. H. Allen-Sutter, E. Garhart, K. Leinenweber, V. Prakapenka, E. Greenberg, S.-H. Shim, Oxidation of the interiors of carbide exoplanets. *Planet. Sci. J.* **1**, 39 (2020).
12. D. K. Bradley, J. H. Eggert, R. F. Smith, S. T. Prisbrey, D. G. Hicks, D. G. Braun, J. Biener, A. V. Hamza, R. E. Rudd, G. W. Collins, Diamond at 800 GPa. *Phys. Rev. Lett.* **102**, 075503 (2009).
13. K. Katagiri, N. Ozaki, Y. Umeda, T. Irifune, N. Kamimura, K. Miyanishi, T. Sano, T. Sekine, R. Kodama, Shock response of full density nanopolycrystalline diamond. *Phys. Rev. Lett.* **125**, 185701 (2020).
14. J. M. Lang, Y. M. Gupta, Experimental determination of third-order elastic constants of diamond. *Phys. Rev. Lett.* **106**, 125502 (2011).
15. R. F. Smith, J. H. Eggert, R. Jeanloz, T. S. Duffy, D. G. Braun, J. R. Patterson, R. E. Rudd, J. Biener, A. E. Lazicki, A. V. Hamza, J. Wang, T. Braun, L. X. Benedict, P. M. Celliers, G. W. Collins, Ramp compression of diamond to five terapascals. *Nature* **511**, 330–333 (2014).
16. H. Tang, X. H. Yuan, Y. Cheng, H. Z. Fei, F. Y. Liu, T. Liang, Z. D. Zeng, T. Ishii, M. S. Wang, T. Katsura, H. W. Sheng, H. Y. Gou, Synthesis of paracrystalline diamond. *Nature* **599**, 605–610 (2021).
17. H. K. Mao, R. J. Hemley, Optical-transitions in diamond at ultrahigh pressures. *Nature* **351**, 721–724 (1991).
18. R. J. Hemley, H. K. Mao, G. Y. Shen, J. Badro, P. Gillet, M. Hanfland, D. Hausermann, X-ray imaging of stress and strain of diamond, iron, and tungsten at megabar pressures. *Science* **276**, 1242–1245 (1997).
19. S. S. Lobanov, V. B. Prakapenka, C. Prescher, Z. Konôpková, H.-P. Liermann, K. L. Crispin, C. Zhang, A. F. Goncharov, Pressure, stress, and strain distribution in the double-stage diamond anvil cell. *J. Appl. Phys.* **118**, 035905 (2015).
20. A. L. Ruoff, H. Luo, Y. K. Vohra, The closing diamond anvil optical window in multimegabar research. *J. Appl. Phys.* **69**, 6413–6416 (1991).
21. W. L. Mao, H. K. Mao, P. J. Eng, T. P. Trainor, M. Newville, C. C. Kao, D. L. Heinz, J. F. Shu, Y. Meng, R. J. Hemley, Bonding changes in compressed superhard graphite. *Science* **302**, 425–427 (2003).
22. S. K. Lee, P. J. Eng, H. K. Mao, Probing of pressure-induced bonding transitions in crystalline and amorphous Earth materials: Insights from X-ray Raman scattering at high pressure, in *Spectroscopic Methods in Mineralology and Materials Sciences,* G. S. Henderson, D. R. Neuville, R. T. Downs, Eds. (Reviews in Mineralogy and Geochemistry, Mineralogical Society of America, 2014), vol. 78, pp. 139–174.
23. C. Sternemann, M. Wilke, Spectroscopy of low and intermediate *Z* elements at extreme conditions: *In situ* studies of Earth materials at pressure and temperature via X-ray Raman scattering. *High Pressure Res.* **36**, 275–292 (2016).
24. Y. S. Yi, H. Khim, Y. H. Kim, S. K. Lee, Spectral proxies for bonding transitions in SiO_2 and $MgSiO_3$ polymorphs at high pressure up to 270 GPa by O *K*-edge x-ray Raman scattering. *Phys. Rev. B* **103**, 214109 (2021).
25. Y. Q. Cai, H. K. Mao, P. C. Chow, J. S. Tse, Y. Ma, S. Patchkovskii, J. F. Shu, V. Struzhkin, R. J. Hemley, H. Ishii, C. C. Chen, I. Jarrige, C. T. Chen, S. R. Shieh, E. P. Huang, C. C. Kao, Ordering of hydrogen bonds in high-pressure Low-Temperature H2O. *Phys. Rev. Lett.* **94**, 025502 (2005).
26. W. Schülke, *Electron Dynamics by Inelastic X-ray Scattering* (OUP Oxford, 2007), vol. 7.
27. Y. Lin, L. Zhang, H. K. Mao, P. Chow, Y. M. Xiao, M. Baldini, J. F. Shu, W. L. Mao, Amorphous diamond: A high-pressure superhard carbon allotrope. *Phys. Rev. Lett.* **107**, 175504 (2011).
28. S. K. Lee, Y. H. Kim, Y. S. Yi, P. Chow, Y. M. Xiao, C. Ji, G. Y. Shen, Oxygen quadclusters in SiO_2 glass above megabar pressures up to 160 GPa revealed by x-ray Raman scattering. *Phys. Rev. Lett.* **123**, 235701 (2019).
29. S. K. Lee, Y.-H. Kim, P. Chow, Y. Xiao, C. Ji, G. Shen, Amorphous boron oxide at megabar pressures via inelastic X-ray scattering. *Proc. Natl. Acad. Sci. U.S.A.* **115**, 5855–5860 (2018).
30. Y. H. Kim, Y. S. Yi, H.-I. Kim, P. Chow, Y. Xiao, G. Shen, S. K. Lee, Structural transitions in $MgSiO_3$ glasses and melts at the core-mantle boundary observed *via* inelastic x-ray scattering. *Geophys. Res. Lett.* **46**, 13756–13764 (2019).
31. G. Y. Shen, Y. B. Wang, A. Dewaele, C. Wu, D. E. Fratanduono, J. Eggert, S. Klotz, K. F. Dziubek, P. Loubeyre, O. V. Fat'yanov, P. D. Asimow, T. Mashimo, R. M. M. Wentzcovitch, J. Bass, Y. Bi, D. W. He, K. V. Khishchenko, K. Leinenweber, B. S. Li, T. Sakai, T. Tsuchiya, K. Shimizu, D. Yamazaki, M. Mezouar; other members of the IPPS task group, Toward an international practical pressure scale: A proposal for an IPPS ruby gauge (IPPS-Ruby2020). *High Pressure Res.* **40**, 299–314 (2020).
32. J. F. Morar, F. J. Himpsel, G. Hollinger, G. Hughes, J. L. Jordan, Observation of a C-1s Core exciton in diamond. *Phys. Rev. Lett.* **54**, 1960–1963 (1985).
33. J. Nithianandam, Synchrotron x-ray photoemission and reflectance study of the dipole forbidden diamond core exciton. *Phys. Rev. Lett.* **69**, 3108–3111 (1992).
34. S. P. Gao, C. J. Pickard, M. C. Payne, J. Zhu, J. Yuan, Theory of core-hole effects in 1s core-level spectroscopy of the first-row elements. *Phys. Rev. B* **77**, 115122 (2008).
35. S. Huotari, T. Pylkkanen, J. A. Soininen, J. J. Kas, K. Hamalainen, G. Monaco, X-ray-Raman-scattering-based EXAFS beyond the dipole limit. *J. Synchrot. Radiat.* **19**, 106–113 (2012).
36. F. J. Himpsel, J. F. Vanderveen, D. E. Eastman, Experimental bulk energy bands for diamond using $h\nu$-dependent photoemission. *Phys. Rev. B* **22**, 1967–1971 (1980).
37. F. Occelli, P. Loubeyre, R. LeToullec, Properties of diamond under hydrostatic pressures up to 140 GPa. *Nat. Mater.* **2**, 151–154 (2003).
38. F. Zhi-Jian, J. Guang-Fu, C. Xiang-Rong, G. Qing-Quan, First-principle calculations for elastic and thermodynamic properties of diamond. *Commun. Theor. Phys.* **51**, 1129–1134 (2009).
39. F. Gao, J. He, E. Wu, S. Liu, D. Yu, D. Li, S. Zhang, Y. Tian, Hardness of covalent crystals. *Phys. Rev. Lett.* **91**, 015502 (2003).
40. F. M. Gao, L. H. Gao, Microscopic models of hardness. *J. Superhard Mater.* **32**, 148–166 (2010).
41. A. Mansouri Tehrani, J. Brgoch, Hard and superhard materials: A computational perspective. *J. Solid State Chem.* **271**, 47–58 (2019).
42. V. A. Mukhanov, O. O. Kurakevych, V. L. Solozhenko, Thermodynamic model of hardness: Particular case of boron-rich solids. *J. Superhard Mater.* **32**, 167–176 (2010).
43. V. L. Solozhenko, E. Gregoryanz, Synthesis of superhard materials. *Mater. Today* **8**, 44–51 (2005).
44. J. S. Tse, Intrinsic hardness of crystalline solids. *J. Superhard Mater.* **32**, 177–191 (2010).
45. M. D. Segall, R. Shah, C. J. Pickard, M. C. Payne, Population analysis of plane-wave electronic structure calculations of bulk materials. *Phys. Rev. B Condens. Matter.* **54**, 16317–16320 (1996).

46. Y. Akahama, H. Kawamura, Diamond anvil Raman gauge in multimegabar pressure range. *High Pressure Res.* **27**, 473–482 (2007).
47. R. Vogelgesang, A. K. Ramdas, S. Rodriguez, M. Grimsditch, T. R. Anthony, Brillouin and Raman scattering in natural and isotopically controlled diamond. *Phys. Rev. B Condens. Matter.* **54**, 3989–3999 (1996).
48. R. Maezono, A. Ma, M. D. Towler, R. J. Needs, Equation of state and raman frequency of diamond from quantum Monte Carlo simulations. *Phys. Rev. Lett.* **98**, 025701 (2007).
49. J. S. Tse, W. B. Holzapfel, Equation of state for diamond in wide ranges of pressure and temperature. *J. Appl. Phys.* **104**, 043525 (2008).
50. P. Chow, Y. M. Xiao, E. Rod, L. G. Bai, G. Y. Shen, S. Sinogeikin, N. Gao, Y. Ding, H.-K. Mao, Focusing polycapillary to reduce parasitic scattering for inelastic x-ray measurements at high pressure. *Rev. Sci. Instrum.* **86**, 072203 (2015).
51. Y. H. Kim, Y. S. Yi, H.-I. Kim, P. Chow, Y. Xiao, G. Shen, S. K. Lee, Pressure-driven changes in the electronic bonding environment of GeO_2 glass above megabar pressures. *J. Am. Chem. Soc.* **144**, 10025–10033 (2022).
52. S. J. Clark, M. D. Segall, C. J. Pickard, P. J. Hasnip, M. I. J. Probert, K. Refson, M. C. Payne, First principles methods using CASTEP. *Z. Kristallogr. Cryst. Mater.* **220**, 567–570 (2005).
53. J. P. Perdew, K. Burke, M. Ernzerhof, Generalized gradient approximation made simple. *Phys. Rev. Lett.* **77**, 3865–3868 (1996).
54. Y. S. Yi, S. K. Lee, Atomistic origins of pressure-induced changes in the O *K*-edge x-ray Raman scattering features of Si O_2 and MgSi O_3 polymorphs: Insights from *ab initio* calculations. *Phys. Rev. B* **94**, 094110 (2016).
55. I. Mosyagin, D. Gambino, D. G. Sangiovanni, I. A. Abrikosov, N. M. Caffrey, Effect of dispersion corrections on *ab initio* predictions of graphite and diamond properties under pressure. *Phys. Rev. B* **98**, 174103 (2018).
56. J.-P. Rueff, A. Shukla, Inelastic x-ray scattering by electronic excitations under high pressure. *Rev. Mod. Phys.* **82**, 847 (2010).
57. P. Blaha, K. Schwarz, F. Tran, R. Laskowski, G. K. H. Madsen, L. D. Marks, WIEN2k: An APW+lo program for calculating the properties of solids. *J. Chem. Phys.* **152**, 074101 (2020).
58. T. Mizoguchi, I. Tanaka, S.-P. Gao, C. J. Pickard, First-principles calculation of spectral features, chemical shift and absolute threshold of ELNES and XANES using a plane wave pseudopotential method. *J. Phys. Condens. Matter* **21**, 104204 (2009).
59. J. Zemann, *Crystal Structures, 2nd edition, Vol. 1 by R. W. G. Wyckoff* (Acta Crystallographica, 1965), vol. 18, pp. 139.
60. M. P. Surh, S. G. Louie, M. L. Cohen, Band gaps of diamond under anisotropic stress. *Phys. Rev. B Condens Matter.* **45**, 8239–8247 (1992).
61. A. L. Ruoff, H. Luo, Pressure strengthening: A possible route to obtaining 9 Mbar and metallic diamonds. *J. Appl. Phys.* **70**, 2066–2070 (1991).
62. G. Bertoni, L. Calmels, A. Altibelli, V. Serin, First-principles calculation of the electronic structure and EELS spectra at the graphene/Ni(111) interface. *Phys. Rev. B* **71**, 075402 (2005).
63. Y. Meng, H.-K. Mao, P. J. Eng, T. P. Trainor, M. Newville, M. Y. Hu, C. Kao, J. Shu, D. Hausermann, R. J. Hemley, The formation of sp^3 bonding in compressed BN. *Nat. Mater.* **3**, 111–114 (2004).
64. W. Pabst, E. Gregorova, Elastic properties of silica polymorphs—A review. *Ceramics - Silikaty* **57**, 167–184 (2013).
65. D. Andrault, G. Fiquet, F. Guyot, M. Hanfland, Pressure-induced Landau-type transition in stishovite. *Science* **282**, 720–724 (1998).
66. L.-G. Liu, Bulk moduli of SiO_2 polymorphs: Quartz, coesite and stishovite. *Mech. Mater.* **14**, 283–290 (1993).
67. A. R. Oganov, M. J. Gillan, G. D. Price, Structural stability of silica at high pressures and temperatures. *Phys. Rev. B* **71**, 064104 (2005).
68. Z. Zhang, L. Stixrude, J. Brodholt, Elastic properties of $MgSiO_3$-perovskite under lower mantle conditions and the composition of the deep Earth. *Earth Planet. Sci. Lett.* **379**, 1–12 (2013).
69. X. Jiang, J. Zhao, X. Jiang, Correlation between hardness and elastic moduli of the covalent crystals. *Comput. Mate. Sci.* **50**, 2287–2290 (2011).
70. F. Gao, Theoretical model of intrinsic hardness. *Phys. Rev. B* **73**, 132104 (2006).
71. K. Li, X. Wang, F. Zhang, D. Xue, Electronegativity identification of novel superhard materials. *Phys. Rev. Lett.* **100**, 235504 (2008).
72. V. A. Mukhanov, O. O. Kurakevych, V. L. Solozhenko, Hardness of materials at high temperature and high pressure. *Philos. Mag.* **89**, 2117–2127 (2009).
73. Q. Zhu, A. R. Oganov, M. A. Salvadó, P. Pertierra, A. O. Lyakhov, Denser than diamond: *Ab initio* search for superdense carbon allotropes. *Phys. Rev. B* **83**, 193410 (2011).
74. T. Mizoguchi, Overlap population diagram for ELNES and XANES: Peak assignment and interpretation. *J. Phys. Condens. Matter* **21**, 104215 (2009).
75. A. Šimůnek, J. Vackář, Hardness of covalent and ionic crystals: First-principle calculations. *Phys. Rev. Lett.* **96**, 085501 (2006).
76. S.-Q. Feng, Y. Yang, J.-Y. Li, X.-X. Jiang, H.-N. Li, X.-L. Cheng, Pressure effect on the hardness of diamond and W_2B_5: First-principle calculations. *Mod. Phys. Lett. B* **31**, 1750137 (2017).

Acknowledgments

Funding: This work was supported by the Leader Program of the National Research Foundation of Korea (NRF) (grant no. NRF-2020R1A3B2079815) to S.K.L. HPCAT operations are supported by DOE-NNSA's Office of Experimental Sciences. The Advanced Photon Source is a user facility operated for the DOE Office of Science by Argonne National Laboratory under contract no. DE-AC02-06CH11357. **Author contributions:** S.K.L. conceived and developed the project. S.K.L. and Y.Y. performed ab initio calculations of hydrostatically and uniaxially compressed diamond, respectively. Y.-H.K. prepared DACs and collected IXS spectra. Y.-H.K. and S.K.L. collected 2D IXS image, together with P.C., Y.X., and G.S. S.K.L. and H.-i.K. analyzed the experimental data. Y.Y. and S.K.L. analyzed the theoretical data. S.K.L. wrote the manuscript. Y.Y. contributed the section describing computational methods and uniaxial compression. G.S. and P.E. revised the manuscript. All authors commented on the manuscript. **Competing interests:** The authors declare that they have no competing interests. **Data and materials availability:** All data needed to evaluate the conclusions in the paper are present in the paper and/or the Supplementary Materials.

Submitted 21 December 2022
Accepted 17 April 2023
Published 19 May 2023
10.1126/sciadv.adg4159

ScienceAdvances

Imaging of the electronic bonding of diamond at pressures up to 2 million atmospheres

Sung Keun Lee, Yoosoo Yi, Yong-Hyun Kim, Hyo-im Kim, Paul Chow, Yuming Xiao, Peter Eng, and Guoyin Shen

Sci. Adv. **9** (20), eadg4159. DOI: 10.1126/sciadv.adg4159

Science Advances (ISSN 2375-2548) is published by the American Association for the Advancement of Science. 1200 New York Avenue NW, Washington, DC 20005. The title *Science Advances* is a registered trademark of AAAS.